

# Q-DiT4SR: Exploration of Detail-Preserving Diffusion Transformer Quantization for Real-World Image Super-Resolution

Xun Zhang<sup>1</sup> Kaicheng Yang<sup>1</sup> Hongliang Lu<sup>1</sup> Haotong Qin<sup>2</sup> Yong Guo<sup>3</sup> Yulun Zhang\*<sup>1</sup>

## Abstract

Recently, Diffusion Transformers (DiTs) have emerged in Real-World Image Super-Resolution (Real-ISR) to generate high-quality textures, yet their heavy inference burden hinders real-world deployment. While Post-Training Quantization (PTQ) is a promising solution for acceleration, existing methods in super-resolution mostly focus on U-Net architectures, whereas generic DiT quantization is typically designed for text-to-image tasks. Directly applying these methods to DiT-based super-resolution models leads to severe degradation of local textures. Therefore, we propose **Q-DiT4SR**, the first PTQ framework specifically tailored for DiT-based Real-ISR. We propose **H-SVD**, a hierarchical SVD that integrates a global low-rank branch with a local block-wise rank-1 branch under a matched parameter budget. We further propose **Variance-aware Spatio-Temporal Mixed Precision**: **VaSMP** allocates cross-layer weight bit-widths in a data-free manner based on rate-distortion theory, while **VaTMP** schedules intra-layer activation precision across diffusion timesteps via dynamic programming (DP) with minimal calibration. Experiments on multiple real-world datasets demonstrate that our Q-DiT4SR achieves SOTA performance under both **W4A6** and **W4A4** settings. Notably, the W4A4 quantization configuration reduces model size by **5.8 $\times$**  and computational operations by over **60 $\times$** . Our code and models will be available at <https://github.com/xunzhang1128/Q-DiT4SR>.

## 1. Introduction

Real-world image super-resolution (Real-ISR) aims to restore high-quality images from low-resolution (LR) inputs degraded by complex processes, with applications in medi-

<sup>1</sup>Shanghai Jiao Tong University <sup>2</sup>ETH Zürich <sup>3</sup>Huawei. Correspondence to: Yulun Zhang\* <yulun100@gmail.com>.

Preprint. February 3, 2026.

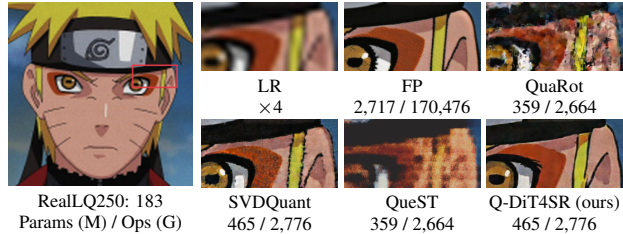


Figure 1. Visual comparison ( $\times 4$ ) under W4A4 setting. Compared with existing quantization methods, our quantized 4-bit Q-DiT4SR better preserves fine-grained textures, while remaining visually close to the full-precision (FP) model. We also provide the parameter (*i.e.*, Params (M)) and operation numbers (*i.e.*, Ops (G)).

cal imaging, satellite reconnaissance, and consumer photography (Wang et al., 2021; 2018; Zhang et al., 2021). Traditional methods have evolved from CNNs (Dong et al., 2014; Kim et al., 2016b; Lim et al., 2017; Zhang et al., 2018c) and Transformers (Liang et al., 2021; Liu et al., 2021; Zamir et al., 2022) to diffusion-based models (Rombach et al., 2022; Ho et al., 2020; Song et al., 2021). State-of-the-art diffusion methods, such as StableSR (Wang et al., 2024), DiffBIR (Lin et al., 2024), and SeeSR (Wu et al., 2024c), demonstrate strong restoration capabilities by jointly leveraging semantic guidance and pixel-aware conditions.

Recent Diffusion Transformers (DiTs) (Peebles & Xie, 2023), built entirely on linear layers and self-attention, achieve superior restoration quality (Duan et al., 2025; Ai et al., 2024; Cheng et al., 2025). However, a typical DiT model is characterized by an extremely large parameter count and heavy computational complexity, accompanied by substantial memory overhead. This computational bottleneck limits the practical deployment of DiT-based SR.

Post-training quantization (PTQ) (Li et al., 2021; Hubara et al., 2021; Nagel et al., 2019) compresses weights and activations with light fine-tuning. However, quantizing diffusion models is challenging: quantization errors accumulate across timesteps (Li et al., 2023a; So et al., 2023), activation distributions vary dramatically (He et al., 2023; Shang et al., 2023), and Real-ISR is sensitive to high-frequency distortions. While recent DiT quantization methods (Wu et al., 2024a; Chen et al., 2025; Li et al., 2024; Yang et al., 2025) have made progress, they either require extensive calibration or suffer quality degradation under aggressive bit-widths (*e.g.*, W4A4), inadequately addressing three key challenges:

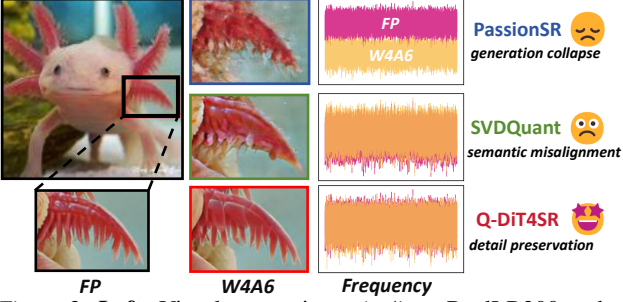


Figure 2. **Left:** Visual comparisons ( $\times 4$ ) on RealLR200 under W4A6. **Right:** Frequency energy of the `blocks.23.ff.net.2` layer outputs from three W4A6 models, compared with the FP model.

(1) Many matrix decomposition approaches overly simplify model representations, making it difficult to retain the fine-grained image details required for texture reconstruction. (2) Despite pronounced inter-layer differences in DiT-based SR models, current mixed-precision quantization methods lack a calibration-free mechanism to assign different weight bit-widths across layers. (3) In diffusion-based Real-ISR, most activation quantization schemes adopt static precision across timesteps, neglecting to exploit temporal dynamics.

To address those challenges, we propose **Q-DiT4SR**, a post-training quantization (PTQ) framework that improves both weight approximation and precision scheduling for efficient DiT-based Real-ISR. We propose **H-SVD** (Hierarchical SVD) that decomposes weights into a global low-rank branch and a local block-wise rank-1 branch under matched parameter budget. We further propose Variance-aware Spatio-Temporal Mixed Precision: **VaSMP** allocates different weight bits across layers in a data-free manner, while **VaTMP** schedules intra-layer activation precision across timesteps. Experiments on real-world benchmarks demonstrate Q-DiT4SR achieves SOTA performance under W4A6 and W4A4 settings (see Fig. 1 and 2). Notably, our W4A4 quantized model reduces size by **5.8 $\times$**  and operations by over **60 $\times$**  compared with the full-precision (FP) version.

Our main contributions are summarized as follows:

- We propose Q-DiT4SR, a PTQ framework for DiT-based Real-ISR. To the best of our knowledge, our Q-DiT4SR is the first attempt to systematically explore aggressive low-bit PTQ for DiT-based Real-ISR.
- We propose H-SVD, a hierarchical SVD weight decomposition strategy, which significantly improves the preservation of fine-grained textures critical for Real-ISR under aggressive low-bit quantization.
- We propose variance-aware spatio-temporal mixed precision: VaSMP for calibration-free cross-layer weight precision allocation, and VaTMP for intra-layer activation precision scheduling across diffusion timesteps.
- Extensive experiments on multiple real-world datasets demonstrate that our Q-DiT4SR achieves SOTA performance under both W4A6 and W4A4 settings.

## 2. Related Work

### 2.1. Image Super-Resolution

Deep learning-based image super-resolution (SR) has evolved from early convolutional neural networks (CNNs) (Dong et al., 2014; Kim et al., 2016b;a) to architectures with residual learning (He et al., 2016; Lim et al., 2017; Zhang et al., 2018a;c) and Transformers (Liang et al., 2021; Chen et al., 2023a;b). For Real-World Image Super-Resolution (Real-ISR), GAN-based methods (Wang et al., 2018; 2021; Liang et al., 2021) pioneer perceptually realistic restoration, while recent breakthroughs leverage latent diffusion models (Rombach et al., 2022). State-of-the-art diffusion-based SR methods, such as StableSR (Wang et al., 2024), DiffBIR (Lin et al., 2024), SeeSR (Wu et al., 2024c) and OSEDiff (Wu et al., 2024b) achieve strong quality via semantic guidance and pixel-aware conditioning. Recent work has demonstrated that Diffusion Transformer (DiT) architectures, such as DiT4SR (Duan et al., 2025) and Dream-Clear (Ai et al., 2024), achieve impressive performance. Notably, traditional SR models rely heavily on convolutional layers, and most existing quantization methods are tailored for such architectures. In contrast, recent DiT-based SR models depend mostly on linear layers, presenting new challenges for efficient low-bit quantization.

### 2.2. Quantization of Diffusion Models

Quantizing diffusion models is challenging due to iterative denoising and activation outliers across timesteps. Quantization-aware training (QAT) approaches (Zhou et al., 2016; Esser et al., 2019; Qin et al., 2023; Zheng et al., 2024; 2025; Yang et al., 2025; Li et al., 2023b) can fine-tune models for low-bit precision but require expensive retraining and large-scale datasets. In contrast, post-training quantization (PTQ) enables deployment with light fine-tuning. Early PTQ methods for general diffusion models, such as Q-Diffusion (Li et al., 2023a) and PTQD (He et al., 2023), adapt calibration strategies for timestep-dependent distributions, while Temporal Dynamic Quantization (So et al., 2023) introduces timestep-aware bit allocation. For Diffusion Transformers (DiTs), PTQ4DiT (Wu et al., 2024a) proposes channel reordering and block reconstruction, and Q-DiT (Chen et al., 2025) introduces window attention-aware rounding. SVDQuant (Li et al., 2024) employs low-rank decomposition to mitigate outliers, enabling 4-bit quantization. RobuQ (Yang et al., 2025) leverages Hadamard transforms for W1.58A2 quantization in DiTs. For SR-specific diffusion models, PassionSR (Zhu et al., 2025) tunes adaptive scales in one-step models. However, most PTQ methods require much calibration data and iterative optimization. In contrast, our approach achieves training-free PTQ with minimal calibration overhead: VaSMP allocates weight precision offline without any calibration, while VaTMP requires only a tiny calibration set for activation precision allocation.

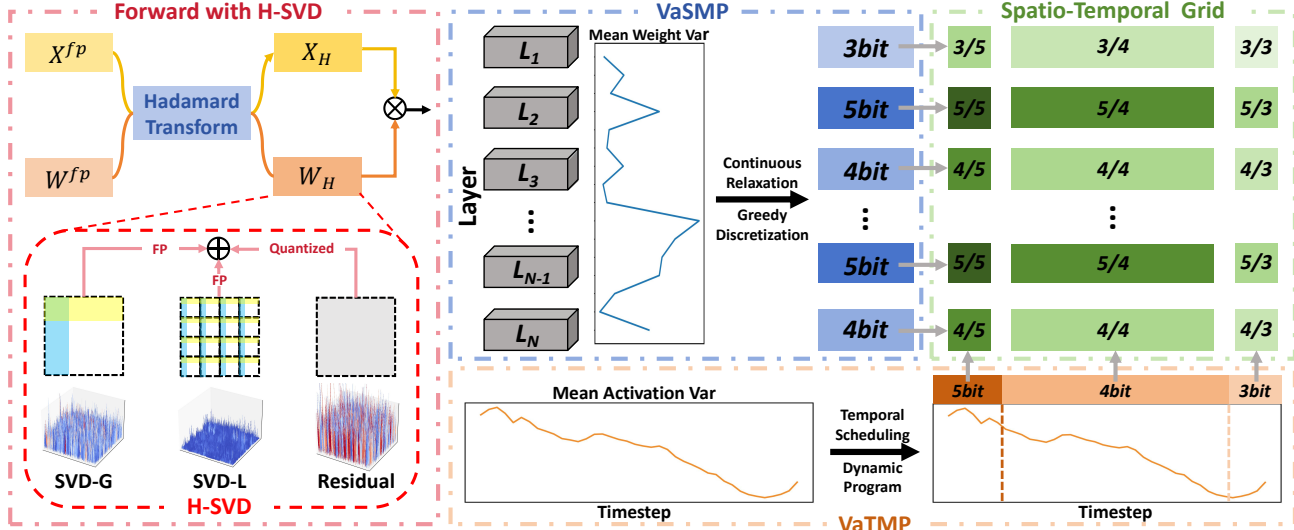


Figure 3. Overview of our proposed Q-DiT4SR framework. (a) Forward with H-SVD: we reconstruct and quantize DiT weights using a hierarchical decomposition that integrates SVD-G with SVD-L. (b) VaSMP: a cross-layer mixed-precision assignment for weights driven by mean weight variance. (c) VaTMP: a intra-layer scheduling that allocates activation precision across diffusion timesteps using mean activation variance. The spatio-temporal grid specifies per-(layer, timestep) bit configurations (weight/activation bit pairs) for deployment.

### 2.3. Mixed-Precision Quantization

Mixed-precision quantization allocates different bit-widths per layer or component to balance accuracy and efficiency. HAWQ (Dong et al., 2019) and its successors (Dong et al., 2020; Yao et al., 2021) use Hessian-based sensitivity for bit allocation, while BRECO (Li et al., 2021) performs block-wise reconstruction. Recent work extends to Transformers and diffusion models: MixDQ (Zhao et al., 2024) decouples metric-based sensitivity for few-step text-to-image models, HQ-DiT (Liu & Zhang, 2024) introduces FP4 hybrid quantization, and MPQ-DM (Feng et al., 2025a) as well as MPQ-DMv2 (Feng et al., 2025b) applies residual mixed-precision with temporal distillation. For large language models (LLMs), IMPQ (Zhao et al., 2025) and AMQ (Lee et al., 2025) enable automated mixed-precision via interaction-aware or AutoML-based strategies. However, most methods require expensive calibration with large datasets or iterative forward passes. In contrast, our VaSMP allocates weight precision offline without any calibration, while VaTMP uses only a tiny calibration set with negligible computation to determine activation precision via variance statistics.

## 3. Method

### 3.1. Preliminaries

**Activation Quantization.** Given activations  $\mathbf{X} \in \mathbb{R}^{T \times C}$ , each token  $\mathbf{x} = \mathbf{X}_{t,:}^\top \in \mathbb{R}^C$  is transformed using a normalized Hadamard matrix  $\mathbf{H}_n$  (Ashkboos et al., 2024; Yang et al., 2025; Tseng et al., 2024; Liu et al., 2025b):  $\mathbf{Z} = \mathbf{X}\mathbf{H}_n$ . Under some assumptions, the transformed activations are approximately Gaussian on a per-token basis,

$$\mathbf{Z}_{t,:} \approx \mathcal{N}(\mathbf{0}, \sigma_t^2 \mathbf{I}), \quad \sigma_t^2 = \frac{1}{C} \|\mathbf{Z}_{t,:}\|_2^2. \quad (1)$$

where  $\sigma_t$  is estimated per token (Yang et al., 2025; Kolb et al., 2023). Quantization is performed using a symmetric

uniform quantizer  $Q_{\text{uni}}(\cdot)$  pre-optimized for  $\mathcal{N}(0, 1)$ :

$$Q_G(\mathbf{x}) = \sigma_t \cdot Q_{\text{uni}}\left(\frac{\mathbf{H}_n^\top \mathbf{x}}{\sigma_t}\right). \quad (2)$$

**Weight Quantization.** For a weight matrix  $\mathbf{W} \in \mathbb{R}^{out \times in}$ , a normalized Hadamard transform is also applied (Ashkboos et al., 2024; Yang et al., 2025; Tseng et al., 2024; Liu et al., 2025b):  $\mathbf{W}_H = \mathbf{W}\mathbf{H}_n$ . A truncated SVD is then computed to retain a rank- $r$  FP low-rank branch  $\mathbf{W}_{\text{LRB}}$  (e.g.,  $r=32$ ) (Yang et al., 2025; Li et al., 2024; Liu et al., 2025a). The residual  $\mathbf{W}_{\text{res}} = \mathbf{W}_H - \mathbf{W}_{\text{LRB}}$  is then quantized using the same uniform quantizer as used for activations:

$$Q_w(\mathbf{W}_{\text{res}}) = \sigma_o \cdot Q_{\text{uni}}\left(\frac{\mathbf{W}_{\text{res}}}{\sigma_o}\right), \quad (3)$$

where  $\sigma_o$  is estimated independently for each output channel. The final weight is then quantized and reconstructed as (Li et al., 2024; Yang et al., 2025; Liu et al., 2025a),

$$\hat{\mathbf{W}} = (\mathbf{W}_{\text{LRB}} + Q_w(\mathbf{W}_{\text{res}})) \mathbf{H}_n^\top. \quad (4)$$

Overall, this framework makes both weights and activations approximately Gaussian, enabling efficient and stable PTQ.

### 3.2. Hierarchical SVD

#### 3.2.1. MOTIVATION

Diffusion-based image SR models are highly sensitive to high-frequency details. Under the quantization backbone (Sec. 3.1), each weight matrix is decomposed into a FP low-rank branch and a quantized residual. While the low-rank component captures dominant global structures, the residual often contains critical high-frequency and local information, making it particularly vulnerable to low-bit quantization.

To better preserve FP information flow, we propose a hierarchical SVD (H-SVD) that integrates a complementary global low-rank branch with a local block-wise rank-1

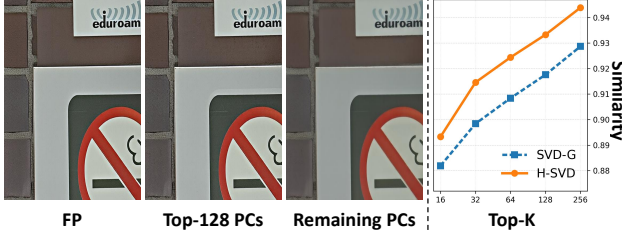


Figure 4. PCA analysis on RealSR Canon\_001. **Left:** Top-128 principal components (PCs) are progressively removed from the output of the `blocks.23.ff.net.2` layer in the FP model. Removing dominant PCs leads to a significant degradation in SR quality, highlighting their importance in SR tasks. **Right:** Comparison between SVD-G and H-SVD under matched parameter budgets for the same non-quantized layer, with outputs projected onto the FP PC space. The hierarchical decomposition aligns more closely with the FP model, demonstrating the effectiveness of H-SVD.

branch in the transformed weight space (Fig. 3 (left)). By jointly modeling global and local structures, H-SVD enables a more faithful approximation of FP weights under a fixed parameter budget. Empirically, as shown in Fig. 4 (left), a small number of principal components (PCs) dominate image SR quality, motivating the allocation of adaptation capacity across both global and local SVD components.

### 3.2.2. GLOBAL SVD CONSTRUCTION

Following Sec. 3.1, we first apply a Hadamard transform to the weight matrix to obtain a more balanced distribution:  $\mathbf{W}_H = \mathbf{W}\mathbf{H}_n$ . We then perform a truncated SVD on  $\mathbf{W}_H$  to extract a FP global approximation, denoted as  $\mathbf{W}_{\text{SVD-G}}$ . This global branch (SVD-G) captures the dominant low-frequency components of the weight matrix, which are crucial for preserving the overall structural behavior of the FP model. The remaining residual is defined as  $\mathbf{W}_{\text{res}} = \mathbf{W}_H - \mathbf{W}_{\text{SVD-G}}$ , which primarily contains fine-grained and local information that is difficult to approximate using a single global low-rank branch alone.

### 3.2.3. LOCAL SVD CONSTRUCTION

Given the residual weight  $\mathbf{W}_{\text{res}} \in \mathbb{R}^{out \times in}$ , we construct a local SVD branch (SVD-L) by partitioning  $\mathbf{W}_{\text{res}}$  into some non-overlapping blocks of size  $s_o \times s_i$ . This yields  $B = \frac{out}{s_o} \cdot \frac{in}{s_i}$  small blocks  $\mathbf{W}^{(p,q)} \in \mathbb{R}^{s_o \times s_i}$ .

For each block, we apply a rank-1 SVD approximation

$$\mathbf{W}^{(p,q)} \approx \hat{\mathbf{W}}^{(p,q)} = \sigma_{p,q} \mathbf{u}_{p,q} \mathbf{v}_{p,q}^\top, \quad (5)$$

where  $\mathbf{u}_{p,q} \in \mathbb{R}^{s_o}$ ,  $\mathbf{v}_{p,q} \in \mathbb{R}^{s_i}$ , and  $\sigma_{p,q} \in \mathbb{R}_+$  denote the top singular components. All block-wise approximations are assembled to form the local SVD branch

$$\mathbf{W}_{\text{SVD-L}} = \text{Assemble}(\{\hat{\mathbf{W}}^{(p,q)}\}_{p,q}) \in \mathbb{R}^{out \times in}. \quad (6)$$

Let  $r$  denote the target rank used as a unified budget reference. A standard global SVD branch parameterizes  $\mathbf{W}_{\text{SVD-G}} = \mathbf{A}\mathbf{B}$  with  $\mathbf{A} \in \mathbb{R}^{out \times r}$  and  $\mathbf{B} \in \mathbb{R}^{r \times in}$ , leading to a parameter budget  $P_{\text{SVD-G}}(r) = r(out + in)$ . A rank-1 block  $\hat{\mathbf{W}}^{(p,q)}$  requires  $P_{\text{blk}}(s_o, s_i) = s_o + s_i + 1$

parameters, and the total budget of the local branch is

$$P_{\text{SVD-L}}(s_o, s_i) = \frac{out}{s_o} \cdot \frac{in}{s_i} \cdot (s_o + s_i + 1). \quad (7)$$

We search over all feasible block sizes

$$\mathcal{S} = \{(s_o, s_i) : s_o \mid out, s_i \mid in\}, \quad (8)$$

and select a configuration satisfying the constraint

$$P_{\text{SVD-L}}(s_o, s_i) \lesssim P_{\text{SVD-G}}(r), \quad (9)$$

ensuring that SVD-L preserves fine-grained textures while using a parameter budget comparable to rank- $r$  SVD-G.

### 3.2.4. FORWARD COMPUTATION WITH H-SVD

The final weight is reconstructed with H-SVD:

$$\hat{\mathbf{W}} = (\mathbf{W}_{\text{SVD-G}} + \mathbf{W}_{\text{SVD-L}}) \mathbf{H}_n^\top + Q_w(\mathbf{W}_{\text{res}} - \mathbf{W}_{\text{SVD-L}}) \mathbf{H}_n^\top. \quad (10)$$

Accordingly, the forward computation under quantization is

$$\mathbf{y} = Q_w(\mathbf{W}_{\text{res}} - \mathbf{W}_{\text{SVD-L}}) Q_G(\mathbf{x}) + (\mathbf{W}_{\text{SVD-G}} + \mathbf{W}_{\text{SVD-L}}) \mathbf{H}_n^\top \mathbf{x}. \quad (11)$$

By allocating the same parameter budget as a rank- $r$  global SVD branch, H-SVD leverages block-wise rank-1 local structures to better preserve critical residual information. As shown in Fig. 4 (right),  $\mathbf{W}_{\text{SVD-L}}$  retains the dominant components and aligns more closely with the FP model.

## 3.3. Variance-Aware Spatio Mixed Precision

### 3.3.1. MOTIVATION

Consider a scalar random variable  $z \sim \mathcal{N}(0, \sigma^2)$  quantized by a  $b$ -bit symmetric uniform quantizer. Under the standard high-rate approximation, the quantization error satisfies

$$\mathbb{E}[e^2] \propto \sigma^2 2^{-2b}, \quad (12)$$

where the step size scales as  $\Delta = \mathcal{O}(\sigma 2^{-b})$  for a Gaussian source clipped to  $[-\alpha\sigma, \alpha\sigma]$ .

Extending to a Hadamard-transformed weight matrix  $\mathbf{W}_H^{(\ell)}$  in layer  $\ell$ , let  $\mathbf{w}_{\ell,o}$  denote its  $o$ -th output-channel row with variance  $\sigma_{\ell,o}^2$ . Elementwise uniform quantization with bit-width  $b_\ell$  induces a layer-wise distortion

$$D_\ell(b_\ell) \triangleq \mathbb{E}[\|\mathbf{Q}(\mathbf{W}_H^{(\ell)}) - \mathbf{W}_H^{(\ell)}\|_F^2] \propto N_\ell \bar{\sigma}_\ell^2 2^{-2b_\ell}, \quad (13)$$

where  $N_\ell$  is the number of parameters in layer  $\ell$  and  $\bar{\sigma}_\ell^2 = \frac{1}{out_\ell} \sum_{o=1}^{out_\ell} \sigma_{\ell,o}^2$  is the average output-channel variance.

Eq. (13) indicates that, under a shared uniform-quantization design, the expected layer distortion is dominated by  $\bar{\sigma}_\ell^2$ . In Fig. 5, weight variances exhibit strong inter-layer diversity and remain relatively stable within a layer. It motivates an optimal data-free variance-aware spatio mixed precision (VaSMP) strategy that allocates weight bit-widths based on  $\bar{\sigma}_\ell^2$  without any calibration data, as shown in Fig. 3 (middle).

### 3.3.2. BIT ALLOCATION WITH VASMP

**Offline Statistics.** All statistics are collected offline without any calibration data. For each layer  $\ell$ , we compute the average output-channel variance  $\bar{\sigma}_\ell^2$  and parameter count  $N_\ell$

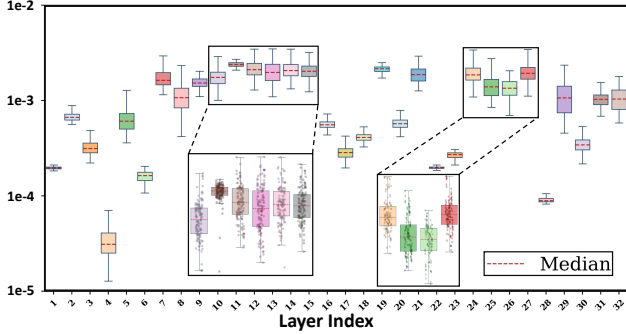


Figure 5. Variance Distribution Analysis. The boxplot is generated by randomly selecting 32 different types of layers and calculating the variance of 128 randomly selected output channels for each layer. The variance of Hadamard-transformed weights varies by orders of magnitude across layers, while remaining relatively stable across output channels within a single layer.

in the Hadamard domain. We define the active set  $\mathcal{A} \triangleq \{\ell : \text{layer } \ell \text{ participates in the forward computation}\}$ .

**Continuous Relaxation.** Motivated by Eq. (13), we minimize the distortion under a target average bit-width  $B_{\text{target}}$ :

$$\begin{aligned} \min_{\{b_\ell\}_{\ell \in \mathcal{A}}} \quad & \sum_{\ell \in \mathcal{A}} N_\ell \bar{\sigma}_\ell^2 2^{-2b_\ell} \\ \text{s.t.} \quad & \sum_{\ell \in \mathcal{A}} w_\ell b_\ell = B_{\text{target}} \sum_{\ell \in \mathcal{A}} w_\ell, \end{aligned} \quad (14)$$

where  $w_\ell = N_\ell$ . Let

$$\log_2 \bar{\sigma} = \frac{\sum_{\ell \in \mathcal{A}} w_\ell \log_2(\max(\bar{\sigma}_\ell^2, \epsilon))}{\sum_{\ell \in \mathcal{A}} w_\ell}, \quad (15)$$

then the optimal continuous solution is

$$b_\ell^* = B_{\text{target}} + \frac{1}{2} (\log_2(\max(\bar{\sigma}_\ell^2, \epsilon)) - \log_2 \bar{\sigma}), \ell \in \mathcal{A}. \quad (16)$$

**Greedy Discretization.** We discretize  $\{b_\ell^*\}$  by initializing  $b_\ell \leftarrow \text{clip}(\lfloor b_\ell^* \rfloor, b_{\min}, b_{\max})$  and greedily allocating remaining bits. From Eq. (13), increasing  $b_\ell$  by one bit reduces the distortion proportionally to  $\text{Gain}_\ell \propto \bar{\sigma}_\ell^2 4^{-b_\ell}$ , which serves as the priority score for bit assignment. The resulting integer bit-widths are used for inference.

### 3.4. Variance-Aware Temporal Mixed Precision

#### 3.4.1. MOTIVATION

Due to different layer families in diffusion SR backbones, cross-layer activation mixed precision is unreliable. After the Hadamard transform, token activations are approximately Gaussian and exhibit a clear temporal variance trend (Fig. 6 (left)). Since uniform quantization distortion scales with variance (Eq. (12)), timestep-wise variance naturally serves as an intra-layer sensitivity indicator. As shown in Fig. 3 (right lower), we therefore propose a variance-aware temporal mixed precision (VaTMP) strategy for activations.

Formally, for token activations  $\mathbf{X}^{(\ell,t)} \in \mathbb{R}^{N \times C}$  at layer  $\ell$  and diffusion timestep  $t$ , we apply  $\mathbf{Z}^{(\ell,t)} = \mathbf{X}^{(\ell,t)} \mathbf{H}_n$ , and define the timestep sensitivity as the mean token variance

$$v_{\ell,t} \triangleq \frac{1}{N \cdot C} \sum_{n=1}^N \|\mathbf{z}_n^{(\ell,t)}\|_2^2, \quad (17)$$

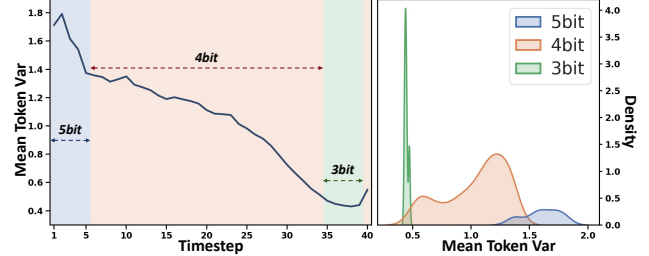


Figure 6. Activation variance and bit-width allocations across diffusion timesteps. **Left:** Evolution of the mean token-wise activation variance over diffusion timesteps, measured on the activations of the `block11.attn2.to_v_control` layer. Background colors indicate the timestep-wise bit-width assignment. **Right:** Kernel density estimation (KDE) of the mean token-wise activation variance, where the shaded area reflects the proportion of timesteps.

where  $\mathbf{z}_n^{(\ell,t)} \in \mathbb{R}^C$  denotes the  $n$ -th token at timestep  $t$ .

#### 3.4.2. BIT ALLOCATION WITH VATMP

We perform timestep-wise activation mixed-precision allocation within each layer after fixing the weight precision (Sec. 3.3, with H-SVD in Sec. 3.2 if enabled). The goal is to minimize activation quantization distortion across diffusion timesteps under a fixed average activation-bit budget.

**Distortion Modeling.** Consider a scalar activation element  $z$  (one channel of one token) at layer  $\ell$  and diffusion timestep  $t$  after the Hadamard transform. We quantize  $z$  using a symmetric uniform quantizer with clipping threshold  $A > 0$  and bit-width  $b \in \mathcal{B}$  (e.g.,  $\mathcal{B} = \{2, 3, 4, 5, 6, 7, 8\}$ ):

$$Q_{A,b}(z) = \Delta \cdot \left\lfloor \frac{\text{clip}(z, -A, A)}{\Delta} \right\rfloor, \quad \Delta = \frac{2A}{2^b - 1}. \quad (18)$$

Here  $\text{clip}(z, -A, A) = \min(\max(z, -A), A)$  and  $\lfloor \cdot \rfloor$  denotes rounding-to-nearest. Following the Gaussian assumption (Sec. 3.1), we model  $z \sim \mathcal{N}(0, v_{\ell,t})$ . Let  $Z \sim \mathcal{N}(0, 1)$  and write  $z = \sqrt{v_{\ell,t}} Z$ . We define a normalized distortion coefficient on  $\mathcal{N}(0, 1)$  with optimal clipping:

$$\kappa(b) \triangleq \min_{A>0} \mathbb{E}_{Z \sim \mathcal{N}(0,1)} [(Z - Q_{A,b}(Z))^2], \quad b \in \mathcal{B}, \quad (19)$$

and denote the corresponding optimal normalized clipping threshold as  $A^*(b) = \arg \min_{A>0} \mathbb{E}[(Z - Q_{A,b}(Z))^2]$ . In practice, for  $z \sim \mathcal{N}(0, v_{\ell,t})$ , we set the clipping threshold to  $A = \sqrt{v_{\ell,t}} A^*(b)$ . Then the expected distortion satisfies

$$D_{\ell,t}(b) \triangleq \mathbb{E}[(z - Q_{\sqrt{v_{\ell,t}} A^*(b), b}(z))^2] = v_{\ell,t} \kappa(b). \quad (20)$$

**Temporal Scheduling.** For each layer  $\ell$ , we assign timestep-wise activation bits  $\{b_{\ell,t}\}_{t=1}^{T_\ell}$  under an average-bit budget

$$\sum_{t=1}^{T_\ell} b_{\ell,t} \leq B_\ell \triangleq \lfloor B_{\text{target}}^{act} T_\ell \rfloor. \quad (21)$$

We need to minimize the total distortion

$$\min_{\{b_{\ell,t} \in \mathcal{B}\}} \sum_{t=1}^{T_\ell} \kappa(b_{\ell,t}) v_{\ell,t}, \quad \text{s.t.} \quad \sum_{t=1}^{T_\ell} b_{\ell,t} \leq B_\ell, \quad (22)$$

while restricting the solution to piecewise-constant schedules over continuous timestep segments. For a segment  $[i, j)$

Table 1. Quantitative comparison on four real-world benchmarks. Best and second best performance are highlighted in red and blue.

(a) W4A6 setting

Datasets	Metrics	FP	Q-Diffusion ICCV 2023	EfficientDM ICLR 2024	PTQ4DiT NeurIPS 2024	QuaRot NeurIPS 2024	SVDQuant ICLR 2025	Q-DiT CVPR 2025	PassionSR CVPR 2025	FlatQuant ICML 2025	QueST ICCV 2025	Q-DiT4SR
DrealSR	LPIPS ↓	0.3897	0.7045	0.7049	0.4627	0.3925	<b>0.3829</b>	0.6843	0.4774	0.4921	0.8210	<b>0.3880</b>
	MUSIQ ↑	64.69	57.75	59.42	56.83	61.09	<b>61.51</b>	57.01	50.55	53.74	40.11	<b>64.32</b>
	MANIQA ↑	0.4483	0.4185	<b>0.5027</b>	0.3457	0.3875	0.3931	0.4159	0.3041	0.3296	0.3541	<b>0.4378</b>
	ClipIQA ↑	0.5555	0.4200	0.3985	0.4060	0.4876	<b>0.4885</b>	0.3806	0.3705	0.3951	0.3287	<b>0.5492</b>
	LIQE ↑	4.031	1.928	2.057	2.579	3.275	<b>3.344</b>	1.709	2.036	2.340	1.145	<b>3.930</b>
RealSR	LPIPS ↓	0.3179	0.7106	0.7063	0.3928	<b>0.3324</b>	<b>0.3371</b>	0.6855	0.4218	0.4345	0.8656	0.3386
	MUSIQ ↑	67.89	59.63	61.26	59.77	64.47	<b>66.63</b>	59.02	54.85	57.11	45.99	<b>67.72</b>
	MANIQA ↑	0.4620	0.4122	<b>0.5117</b>	0.3496	0.4041	0.4306	0.4344	0.3096	0.3337	0.3624	<b>0.4566</b>
	ClipIQA ↑	0.5482	0.4348	0.4077	0.4239	0.4963	<b>0.5180</b>	0.4002	0.3830	0.4143	0.3350	<b>0.5671</b>
	LIQE ↑	3.988	1.972	2.192	2.656	3.323	<b>3.434</b>	1.790	2.176	2.455	1.047	<b>3.980</b>
RealLR200	MUSIQ ↑	70.33	57.87	58.80	63.25	67.51	<b>68.78</b>	56.78	58.18	59.86	37.46	<b>70.36</b>
	MANIQA ↑	0.4636	0.4067	<b>0.5175</b>	0.3469	0.4121	0.4240	0.4053	0.3001	0.3200	0.2910	<b>0.4635</b>
	ClipIQA ↑	0.5814	0.4247	0.4350	0.4544	0.5226	<b>0.5366</b>	0.4243	0.4096	0.4365	0.3232	<b>0.5851</b>
	LIQE ↑	4.303	1.898	2.199	2.831	3.743	<b>3.922</b>	1.590	2.360	2.655	1.032	<b>4.312</b>
	MUSIQ ↑	71.70	58.91	59.60	63.95	68.95	<b>69.81</b>	58.19	58.82	61.10	36.99	<b>71.46</b>
RealLQ250	MANIQA ↑	0.4614	0.4083	<b>0.5218</b>	0.3284	0.4078	0.4145	0.4047	0.2958	0.3116	0.3104	<b>0.4579</b>
	ClipIQA ↑	0.5744	0.4272	0.4385	0.4258	0.5136	<b>0.5175</b>	0.4280	0.3961	0.4229	0.3329	<b>0.5724</b>
	LIQE ↑	4.332	1.968	2.277	2.806	3.847	<b>3.936</b>	1.624	2.317	2.609	1.035	<b>4.345</b>

(b) W4A4 setting

Datasets	Metrics	FP	Q-Diffusion ICCV 2023	EfficientDM ICLR 2024	PTQ4DiT NeurIPS 2024	QuaRot NeurIPS 2024	SVDQuant ICLR 2025	Q-DiT CVPR 2025	PassionSR CVPR 2025	FlatQuant ICML 2025	QueST ICCV 2025	Q-DiT4SR
DrealSR	LPIPS ↓	0.3897	0.7113	0.7091	0.6970	0.5747	<b>0.3821</b>	0.6748	0.6900	0.6904	0.8322	<b>0.4327</b>
	MUSIQ ↑	64.69	58.44	57.44	59.26	54.47	<b>60.65</b>	57.75	57.48	58.39	40.05	<b>61.86</b>
	MANIQA ↑	0.4483	<b>0.4991</b>	0.4921	<b>0.4949</b>	0.3357	0.3768	0.4228	0.4684	0.4728	0.3515	0.4030
	ClipIQA ↑	0.5555	0.3963	0.3704	0.3968	0.3506	<b>0.4727</b>	0.3953	0.3725	0.3991	0.3253	<b>0.4894</b>
	LIQE ↑	4.031	1.904	1.917	1.960	1.807	<b>3.154</b>	1.856	1.863	1.949	1.156	<b>3.197</b>
RealSR	LPIPS ↓	0.3179	0.7107	0.7126	0.6934	0.5384	<b>0.3268</b>	0.6806	0.6885	0.6871	0.8663	<b>0.3665</b>
	MUSIQ ↑	67.89	60.20	59.84	60.34	57.13	<b>63.14</b>	59.97	58.95	59.41	45.74	<b>66.36</b>
	MANIQA ↑	0.4620	<b>0.5082</b>	0.5023	<b>0.5104</b>	0.3302	0.3864	0.4310	0.4802	0.4741	0.3612	0.4367
	ClipIQA ↑	0.5482	0.4036	0.3748	0.4050	0.3470	<b>0.4729</b>	0.4064	0.3831	0.4083	0.3242	<b>0.4956</b>
	LIQE ↑	3.988	2.003	2.039	2.141	1.844	<b>3.115</b>	2.009	1.958	1.996	1.050	<b>3.179</b>
RealLR200	MUSIQ ↑	70.33	57.95	57.35	57.63	56.34	<b>67.37</b>	58.16	55.96	56.47	37.21	<b>68.98</b>
	MANIQA ↑	0.4636	<b>0.5111</b>	<b>0.5141</b>	0.5070	0.3010	0.4028	0.4267	0.4626	0.4460	0.2897	0.4265
	ClipIQA ↑	0.5814	0.4257	0.4118	0.4204	0.3754	<b>0.5168</b>	0.4266	0.3948	0.4162	0.3122	<b>0.5293</b>
	LIQE ↑	4.303	2.032	2.050	2.130	1.963	<b>3.731</b>	1.959	1.950	1.973	1.033	<b>3.827</b>
	MUSIQ ↑	71.70	58.46	58.03	58.70	57.33	<b>69.05</b>	59.40	57.09	57.76	36.87	<b>69.80</b>
RealLQ250	MANIQA ↑	0.4614	<b>0.5154</b>	<b>0.5190</b>	0.5153	0.3034	0.3939	0.4279	0.4720	0.4566	0.3084	0.3943
	ClipIQA ↑	0.5744	0.4297	0.4166	0.4348	0.3628	<b>0.5053</b>	0.4245	0.3970	0.4194	0.3318	<b>0.5026</b>
	LIQE ↑	4.332	2.111	2.118	2.186	1.985	<b>3.803</b>	2.029	2.018	2.080	1.042	<b>3.766</b>

assigned bit-width  $b$ , the segment cost is

$$\text{SegCost}_\ell(i, j; b) = \kappa(b) \sum_{t=i}^{j-1} v_{\ell, t}. \quad (23)$$

We collect  $\{v_{\ell, t}\}$  on a small low-resolution (LR) calibration set under quantized weights. We solve the resulting segmented scheduling problem via dynamic programming (DP) and deploy the inferred per-timestep activation-bit schedule. This procedure assigns higher precision to high-variance (more sensitive) timesteps and lower precision to low-variance ones, while satisfying the same average activation-bit budget (e.g., 4bits), as shown in Fig. 6 (right).

## 4. Experiments

### 4.1. Settings

We adopt DiT4SR (Duan et al., 2025) as the backbone for all experiments. Quantization and evaluation are performed on top of this model, where all MM-DiT blocks are quantized, while softmax layers are fixed at 8-bit precision for numerical stability. All experiments are conducted at a  $4 \times 4$

scaling factor and run on a single NVIDIA RTX A6000 GPU for both calibration and evaluation.

**Calibration Dataset.** We use an LR-only calibration set randomly sampled from the RealSR training split (32 images, random  $128 \times 128$  crops), and collect activation statistics under the quantized inference pipeline.

**Test Datasets.** Following DiT4SR, we evaluate the models on four widely used real-world benchmarks: DrealSR (Wei et al., 2020), RealSR (Cai et al., 2019), RealLR200 (Wu et al., 2024c), and RealLQ250 (Ai et al., 2024).

**Metrics.** Following DiT4SR, we use both full- and no-reference metrics for evaluation. Specifically, we adopt LPIPS (Zhang et al., 2018b) as a full-reference perceptual metric, and MUSIQ (Ke et al., 2021), MANIQA (Yang et al., 2022), CLIPQA (Wang et al., 2023), and LIQE (Zhang et al., 2023) as no-reference quality metrics.

**Compared Methods.** For PTQ, we select multiple methods: SVDQuant (Li et al., 2024), QuaRot (Ashkboos et al., 2024)

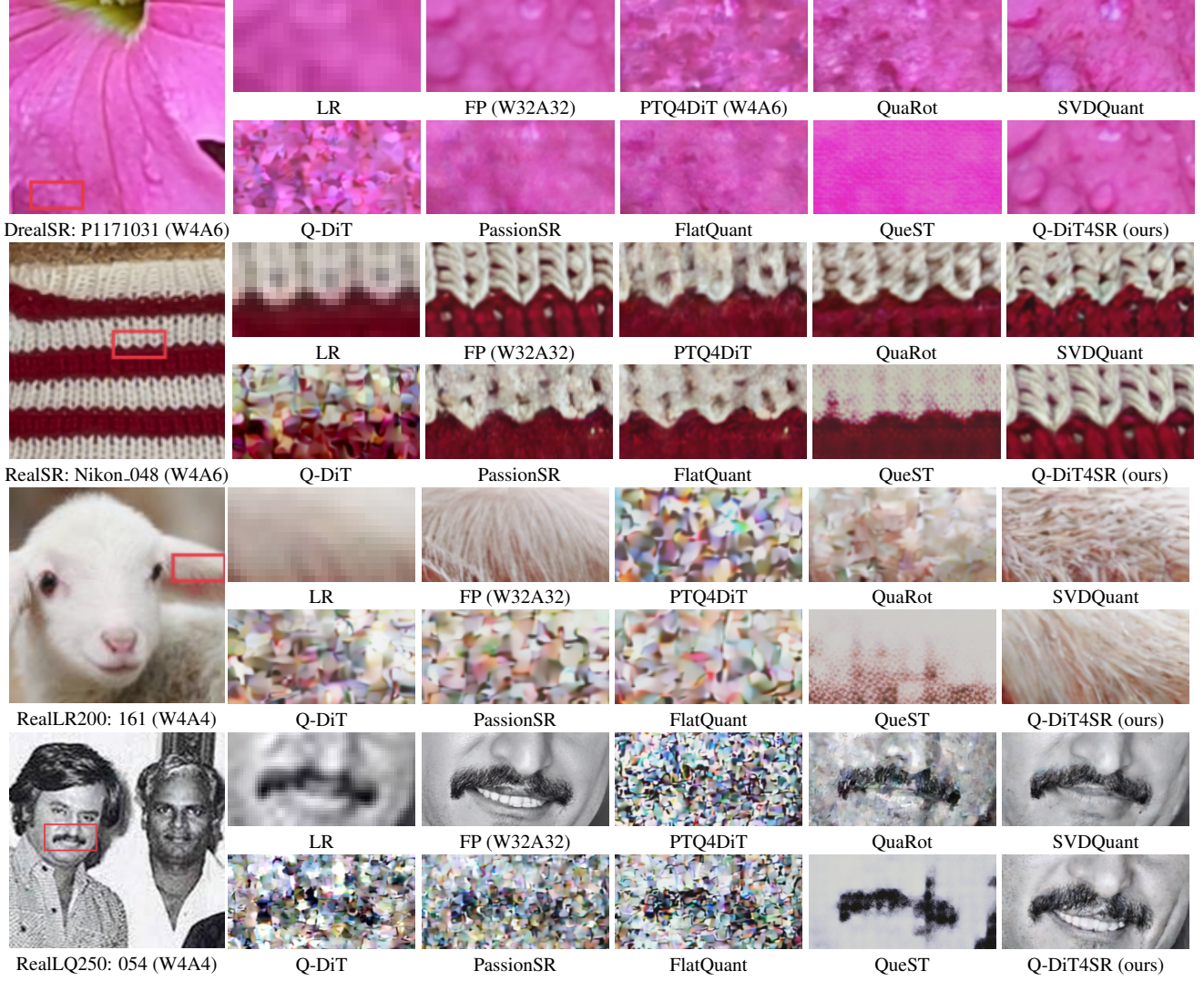


Figure 7. Visual comparisons under W4A6 and W4A4 settings.

Table 2. Ablation study of SVD-L on RealSR under W4A6.

Rank	MUSIQ $\uparrow$	MANIQA $\uparrow$	ClipIQQA $\uparrow$	LIQE $\uparrow$	FLOPs (G)	Param (M)
4	66.71	0.4432	0.5432	3.782	207.37	454.78
8	67.72	0.4566	0.5671	3.980	208.22	465.39
16	67.80	0.4563	0.5447	3.880	209.91	486.62
32	68.01	0.4560	0.5626	3.924	213.28	529.06

and FlatQuant (Sun et al., 2025), DiT-specific approaches Q-DiT (Chen et al., 2025) and PTQ4DiT (Wu et al., 2024a), the diffusion-model method Q-Diffusion (Li et al., 2023a), and the image SR-oriented method PassionSR (Zhu et al., 2025). We also include PEFT methods QueST (Wang et al., 2025) and EfficientDM (He et al., 2024).

## 4.2. Main Results

**Quantitative Results.** Tables 1(a) and (b) report quantitative comparisons with representative quantization methods on four real-world SR benchmarks under W4A6 and W4A4, respectively. Under the W4A6 setting, we disable VaTMP since the activation precision is sufficiently high. Even without temporal mixed precision, Q-DiT4SR achieves very

Table 3. Ablation study of VaSMP on RealSR under W4A6.

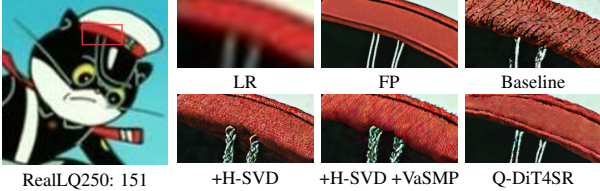
Methods	MUSIQ $\uparrow$	MANIQA $\uparrow$	CLIP-IQA $\uparrow$	LIQE $\uparrow$
Baseline	65.84	0.4286	0.5265	3.696
+H-SVD	67.46	0.4478	0.5475	3.834
+H-SVD +MP	66.84	0.4388	0.5335	3.838
+H-SVD +VaSMP	67.72	0.4566	0.5671	3.980

close performance compared to the FP model across all datasets and metrics, while consistently outperforming prior approaches. Notably, unlike most other methods, Q-DiT4SR requires no calibration data to reach this performance level.

Under the more aggressive W4A4 setting, we further enable VaTMP to mitigate the accumulation of activation quantization error along the diffusion trajectory. As shown in Table 1(b), Q-DiT4SR achieves the best overall performance, whereas existing methods exhibit consistent degradation across datasets and metrics, indicating limited robustness under low activation precision. This highlights that W4A4 constitutes a more challenging regime for DiT backbones, where adaptive activation precision becomes critical.

Table 4. Ablation study of VaTMP on RealSR under W4A4.

Methods	MUSIQ $\uparrow$	MANIQA $\uparrow$	CLIP-IQA $\uparrow$	LIQE $\uparrow$
Baseline	64.94	0.4111	0.4899	3.191
+H-SVD +VaSMP	65.83	0.4227	0.4922	3.091
+H-SVD +VaSMP + VaTMP	66.36	0.4367	0.4956	3.179

Figure 8. Ablation study of H-SVD, VaSMP and VaTMP. Visual comparison ( $\times 4$ ) on RealLQ250 under the W4A4 setting.

We further observe that several methods with visibly noisy reconstructions (e.g. Q-Diffusion and EfficientDM) may still obtain relatively high scores under certain no-reference IQA metrics such as MANIQA. This observation, also reported by PassionSR, suggests a mismatch between perceptual quality and metric responses in heavily quantized diffusion models, motivating future work on more quantization-aware evaluation criteria for diffusion-based SR.

**Visual Comparison.** Figure 7 presents qualitative comparisons on multiple real-world benchmarks under different quantization settings. The first two rows correspond to the W4A6 configuration, while the last two rows are evaluated under the more aggressive W4A4 setting. Across all datasets, our method consistently reconstructs sharper structures and more faithful high-frequency details, exhibiting clearer edges and richer textures than existing quantization baselines. Notably, even under the challenging W4A4 regime, the visual quality produced by our method Q-DiT4SR remains highly competitive, with only marginal perceptual differences compared to the FP model.

### 4.3. Ablation Study

**Rank Budget of SVD-L.** We study the impact of the SVD-L rank budget in H-SVD under W4A6. In all experiments, the SVD-G is fixed to rank 32, and only the SVD-L is varied. As shown in Table 2, increasing the rank budget from 4 to 8 yields the largest performance gain, while further increasing to 16 or 32 brings marginal or even negative improvements. Meanwhile, both FLOPs and parameter counts increase monotonically with the rank budget, indicating a clear quality–efficiency trade-off. Therefore, we set the rank budget of SVD-L to 8 in all subsequent experiments.

**VaSMP.** We evaluate VaSMP under the W4A6 setting on RealSR, with results summarized in Table 3. Starting from the baseline, incorporating H-SVD yields consistent improvements across all metrics. A naive mixed-precision baseline (MP), which allocates weight bit-widths by minimizing a global end-to-end MSE objective, provides only limited gains and may even degrade certain metrics, suggesting that

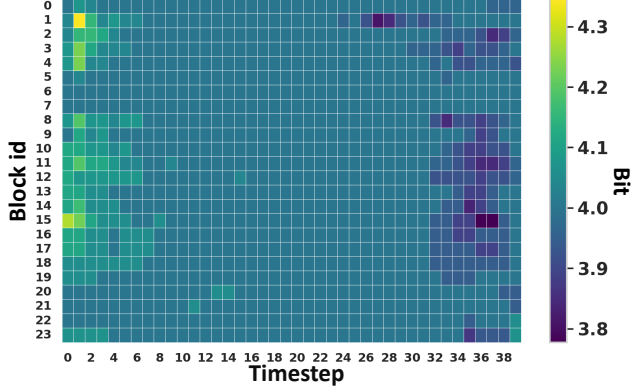


Figure 9. VaTMP scheduling result. Heatmap of the average activation bit-width across DiT blocks and diffusion timesteps.

a purely global criterion fails to capture inter-layer sensitivity differences. In contrast, VaSMP performs cross-layer weight precision allocation guided by weight-variance statistics, explicitly modeling inter-layer variance heterogeneity. This strategy consistently outperforms both H-SVD and MP, achieving the best results across all four IQA metrics.

**VaTMP.** We evaluate VaTMP under the aggressive W4A4 setting on RealSR, with results reported in Table 4. Starting from the W4A4 baseline, combining H-SVD with VaSMP already improves perceptual quality, showing that stronger weight reconstruction and variance-aware weight precision allocation remain effective even under low activation precision. Building on this, VaTMP performs variance-guided temporal activation bit-width allocation across diffusion timesteps, adapting precision to temporal sensitivity. This temporal scheduling consistently brings further gains over H-SVD and VaSMP, achieving the best overall performance. Visual comparisons in Fig. 8 further demonstrate that VaTMP better preserves fine-grained textures and local structures under the same W4A4 budget. The resulting VaTMP scheduling pattern is visualized in Fig. 9.

## 5. Conclusion

We propose Q-DiT4SR, the first post-training quantization (PTQ) framework tailored for efficient deployment of Diffusion Transformers (DiTs) in Real-World Image Super-Resolution (Real-ISR). To preserve fine-grained structures under low-bit precision, we propose H-SVD, a hierarchical weight reconstruction strategy that integrates a global low-rank branch with a local rank-1 branch under a matched parameter budget. We further introduce variance-aware spatio-temporal mixed precision, where VaSMP allocates weight bit-widths across layers in a data-free manner, and VaTMP schedules activation precision across diffusion timesteps. Extensive experiments on multiple real-world benchmarks demonstrate that Q-DiT4SR achieves SOTA performance under both W4A6 and W4A4 settings. We hope this work will facilitate efficient deployment of DiT backbones in resource-constrained Real-ISR applications.

## References

Ai, Y., Zhou, X., Huang, H., Han, X., Chen, Z., You, Q., and Yang, H. Dreamclear: High-capacity real-world image restoration with privacy-safe dataset curation. *NeurIPS*, 2024. [1](#), [2](#), [6](#)

Ashkboos, S., Mohtashami, A., Croci, M. L., Li, B., Cameron, P., Jaggi, M., Alistarh, D., Hoefler, T., and Hensman, J. Quarot: Outlier-free 4-bit inference in rotated llms. In *NeurIPS*, 2024. [3](#), [6](#)

Cai, J., Zeng, H., Yong, H., Cao, Z., and Zhang, L. Toward real-world single image super-resolution: A new benchmark and a new model. In *ICCV*, 2019. [6](#)

Chen, L., Meng, Y., Tang, C., Ma, X., Jiang, J., Wang, X., Wang, Z., and Zhu, W. Q-dit: Accurate post-training quantization for diffusion transformers. In *CVPR*, 2025. [1](#), [2](#), [7](#)

Chen, X., Wang, X., Zhou, J., Qiao, Y., and Dong, C. Activating more pixels in image super-resolution transformer. In *CVPR*, 2023a. [2](#)

Chen, Z., Zhang, Y., Gu, J., Kong, L., Yang, X., and Yu, F. Dual aggregation transformer for image super-resolution. In *ICCV*, 2023b. [2](#)

Cheng, K., Yu, L., Tu, Z., He, X., Chen, L., Guo, Y., Zhu, M., Wang, N., Gao, X., and Hu, J. Effective diffusion transformer architecture for image super-resolution. In *AAAI*, 2025. [1](#)

Dong, C., Loy, C. C., He, K., and Tang, X. Learning a deep convolutional network for image super-resolution. In *ECCV*, 2014. [1](#), [2](#)

Dong, Z., Yao, Z., Gholami, A., Mahoney, M. W., and Keutzer, K. Hawq: Hessian aware quantization of neural networks with mixed-precision. In *ICCV*, 2019. [3](#)

Dong, Z., Yao, Z., Arfeen, D., Gholami, A., Mahoney, M. W., and Keutzer, K. Hawq-v2: Hessian aware trace-weighted quantization of neural networks. In *NeurIPS*, 2020. [3](#)

Duan, Z.-P., Zhang, J., Jin, X., Zhang, Z., Xiong, Z., Zou, D., Ren, J. S., Guo, C., and Li, C. Dit4sr: Taming diffusion transformer for real-world image super-resolution. In *ICCV*, 2025. [1](#), [2](#), [6](#)

Esser, S. K., McKinstry, J. L., Bablani, D., Appuswamy, R., and Modha, D. S. Learned step size quantization. *arXiv preprint arXiv:1902.08153*, 2019. [2](#)

Feng, W., Qin, H., Yang, C., An, Z., Huang, L., Diao, B., Wang, F., Tao, R., Xu, Y., and Magno, M. Mpq-dm: Mixed precision quantization for extremely low bit diffusion models. In *AAAI*, 2025a. [3](#)

Feng, W., Yang, C., Qin, H., Li, Y., Li, X., An, Z., Huang, L., Diao, B., Zhuang, F., Magno, M., et al. Mpq-dmv2: Flexible residual mixed precision quantization for low-bit diffusion models with temporal distillation. *arXiv preprint arXiv:2507.04290*, 2025b. [3](#)

He, K., Zhang, X., Ren, S., and Sun, J. Deep residual learning for image recognition. In *CVPR*, 2016. [2](#)

He, Y., Liu, L., Liu, J., Wu, W., Zhou, H., and Zhuang, B. Ptqd: Accurate post-training quantization for diffusion models. *arXiv preprint arXiv:2305.10657*, 2023. [1](#), [2](#)

He, Y., Liu, J., Wu, W., Zhou, H., and Zhuang, B. Efficientdm: Efficient quantization-aware fine-tuning of low-bit diffusion models. In *ICLR*, 2024. [7](#)

Ho, J., Jain, A., and Abbeel, P. Denoising diffusion probabilistic models. In *NeurIPS*, 2020. [1](#)

Hubara, I., Nahshan, Y., Hanani, Y., Banner, R., and Soudry, D. Accurate post training quantization with small calibration sets. In *ICML*, 2021. [1](#)

Ke, J., Wang, Q., Wang, Y., Milanfar, P., and Yang, F. Musiq: Multi-scale image quality transformer. In *ICCV*, 2021. [6](#)

Kim, J., Kwon Lee, J., and Mu Lee, K. Deeply-recursive convolutional network for image super-resolution. In *CVPR*, 2016a. [2](#)

Kim, J., Lee, J. K., and Lee, K. M. Accurate image super-resolution using very deep convolutional networks. In *CVPR*, 2016b. [1](#), [2](#)

Kolb, C., Müller, C. L., Bischl, B., and Rügamer, D. Smoothing the edges: Smooth optimization for sparse regularization using hadamard overparametrization. In *arXiv preprint arXiv:2307.03571*, 2023. [3](#)

Lee, S., Woo, S.-t., Jin, J.-g., Lee, C., and Park, E. Amq: Enabling automl for mixed-precision weight-only quantization of large language models. In *EMNLP*, 2025. [3](#)

Li, M., Lin, Y., Zhang, Z., Cai, T., Li, X., Guo, J., Xie, E., Meng, C., Zhu, J.-Y., and Han, S. Svdquant: Absorbing outliers by low-rank components for 4-bit diffusion models. *arXiv preprint arXiv:2411.05007*, 2024. [1](#), [2](#), [3](#), [6](#)

Li, X., Liu, Y., Lian, L., Yang, H., Dong, Z., Kang, D., Zhang, S., and Keutzer, K. Q-diffusion: Quantizing diffusion models. In *ICCV*, 2023a. [1](#), [2](#), [7](#)

Li, Y., Gong, R., Tan, X., Yang, Y., Hu, P., Zhang, Q., Yu, F., Wang, W., and Gu, S. Brecq: Pushing the limit of post-training quantization by block reconstruction. *arXiv preprint arXiv:2102.05426*, 2021. [1](#), [3](#)

Li, Y., Xu, S., Cao, X., Sun, X., and Zhang, B. Q-dm: An efficient low-bit quantized diffusion model. In *NeurIPS*, 2023b. [2](#)

Liang, J., Cao, J., Sun, G., Zhang, K., Van Gool, L., and Timofte, R. Swinir: Image restoration using swin transformer. In *ICCV*, 2021. [1](#), [2](#)

Lim, B., Son, S., Kim, H., Nah, S., and Mu Lee, K. Enhanced deep residual networks for single image super-resolution. In *CVPRW*, 2017. [1](#), [2](#)

Lin, X., He, J., Chen, Z., Lyu, Z., Dai, B., Yu, F., Qiao, Y., Ouyang, W., and Dong, C. Diffbir: Toward blind image restoration with generative diffusion prior. In *ECCV*, 2024. [1](#), [2](#)

Liu, K., Yang, K., Chen, Z., Li, Z., Guo, Y., Li, W., Kong, L., and Zhang, Y. Bimacosr: Binary one-step diffusion model leveraging flexible matrix compression for real super-resolution. In *ICML*, 2025a. [3](#)

Liu, W. and Zhang, S. Q. Hq-dit: Efficient diffusion transformer with fp4 hybrid quantization. *arXiv preprint arXiv:2405.19751*, 2024. [3](#)

Liu, Z., Lin, Y., Cao, Y., Hu, H., Wei, Y., Zhang, Z., Lin, S., and Guo, B. Swin transformer: Hierarchical vision transformer using shifted windows. In *ICCV*, 2021. [1](#)

Liu, Z., Zhao, C., Fedorov, I., Soran, B., Choudhary, D., Krishnamoorthi, R., Chandra, V., Tian, Y., and Blankevoort, T. Spinquant: Llm quantization with learned rotations. In *ICLR*, 2025b. [3](#)

Nagel, M., Baalen, M. v., Blankevoort, T., and Welling, M. Data-free quantization through weight equalization and bias correction. In *ICCV*, 2019. [1](#)

Peebles, W. and Xie, S. Scalable diffusion models with transformers. In *ICCV*, 2023. [1](#)

Qin, H., Zhang, Y., Ding, Y., Liu, X., Danelljan, M., Yu, F., et al. Quantsr: accurate low-bit quantization for efficient image super-resolution. In *NeurIPS*, 2023. [2](#)

Rombach, R., Blattmann, A., Lorenz, D., Esser, P., and Ommer, B. High-resolution image synthesis with latent diffusion models. In *CVPR*, 2022. [1](#), [2](#)

Shang, Y., Yuan, Z., Xie, B., Wu, B., and Yan, Y. Post-training quantization on diffusion models. In *CVPR*, 2023. [1](#)

So, J., Lee, J., Ahn, D., Kim, H., and Park, E. Temporal dynamic quantization for diffusion models. *NeurIPS*, 2023. [1](#), [2](#)

Song, Y., Sohl-Dickstein, J., Kingma, D. P., Kumar, A., Ermon, S., and Poole, B. Score-based generative modeling through stochastic differential equations. In *ICLR*, 2021. [1](#)

Sun, Y., Liu, R., Bai, H., Bao, H., Zhao, K., Li, Y., Hu, J., Yu, X., Hou, L., Yuan, C., et al. Flatquant: Flatness matters for llm quantization. In *ICML*, 2025. [7](#)

Tseng, A., Chee, J., Sun, Q., Kuleshov, V., and De Sa, C. Quip#: Even better llm quantization with hadamard incoherence and lattice codebooks. In *ICML*, 2024. [3](#)

Wang, H., Shang, Y., Yuan, Z., Wu, J., Yan, J., and Yan, Y. Quest: Low-bit diffusion model quantization via efficient selective finetuning. In *ICCV*, 2025. [7](#)

Wang, J., Chan, K. C., and Loy, C. C. Exploring clip for assessing the look and feel of images. In *AAAI*, 2023. [6](#)

Wang, J., Yue, Z., Zhou, S., Chan, K. C., and Loy, C. C. Exploiting diffusion prior for real-world image super-resolution. *IJCV*, 2024. [1](#), [2](#)

Wang, X., Yu, K., Wu, S., Gu, J., Liu, Y., Dong, C., Qiao, Y., and Change Loy, C. Esrgan: Enhanced super-resolution generative adversarial networks. In *ECCVW*, 2018. [1](#), [2](#)

Wang, X., Xie, L., Dong, C., and Shan, Y. Real-esrgan: Training real-world blind super-resolution with pure synthetic data. In *ICCV*, 2021. [1](#), [2](#)

Wei, P., Xie, Z., Lu, H., Zhan, Z., Ye, Q., Zuo, W., and Lin, L. Component divide-and-conquer for real-world image super-resolution. In *ECCV*, 2020. [6](#)

Wu, J., Wang, H., Shang, Y., Shah, M., and Yan, Y. Ptq4dit: Post-training quantization for diffusion transformers. In *NeurIPS*, 2024a. [1](#), [2](#), [7](#)

Wu, R., Sun, L., Ma, Z., and Zhang, L. One-step effective diffusion network for real-world image super-resolution. *NeurIPS*, 2024b. [2](#)

Wu, R., Yang, T., Sun, L., Zhang, Z., Li, S., and Zhang, L. Seesr: Towards semantics-aware real-world image super-resolution. In *CVPR*, 2024c. [1](#), [2](#), [6](#)

Yang, K., Zhang, X., Qin, H., Lin, Y., Yang, K., Yan, X., and Zhang, Y. Robuq: Pushing dits to w1. 58a2 via robust activation quantization. *arXiv preprint arXiv:2509.23582*, 2025. [1](#), [2](#), [3](#)

Yang, S., Wu, T., Shi, S., Lao, S., Gong, Y., Cao, M., Wang, J., and Yang, Y. Maniqa: Multi-dimension attention network for no-reference image quality assessment. In *CVPR*, 2022. [6](#)

Yao, Z., Dong, Z., Zheng, Z., Gholami, A., Yu, J., Tan, E., Wang, L., Huang, Q., Wang, Y., Mahoney, M., et al. Hawq-v3: Dyadic neural network quantization. In *ICML*, 2021. [3](#)

Zamir, S. W., Arora, A., Khan, S., Hayat, M., Khan, F. S., and Yang, M.-H. Restormer: Efficient transformer for high-resolution image restoration. In *CVPR*, 2022. [1](#)

Zhang, K., Zuo, W., and Zhang, L. Learning a single convolutional super-resolution network for multiple degradations. In *CVPR*, 2018a. [2](#)

Zhang, K., Liang, J., Van Gool, L., and Timofte, R. Designing a practical degradation model for deep blind image super-resolution. In *ICCV*, 2021. [1](#)

Zhang, R., Isola, P., Efros, A. A., Shechtman, E., and Wang, O. The unreasonable effectiveness of deep features as a perceptual metric. In *CVPR*, 2018b. [6](#)

Zhang, W., Zhai, G., Wei, Y., Yang, X., and Ma, K. Blind image quality assessment via vision-language correspondence: A multitask learning perspective. In *CVPR*, 2023. [6](#)

Zhang, Y., Tian, Y., Kong, Y., Zhong, B., and Fu, Y. Residual dense network for image super-resolution. In *CVPR*, 2018c. [1](#), [2](#)

Zhao, J., Derakhshan, A., Bharadwaj, D., Kana Hyman, J., Dong, J., Abdu Jyothi, S., and Harris, I. Impq: Interaction-aware layerwise mixed precision quantization for llms. *arXiv preprint arXiv:2509.15455*, 2025. [3](#)

Zhao, T., Ning, X., Fang, T., Liu, E., Huang, G., Lin, Z., Yan, S., Dai, G., and Wang, Y. Mixdq: Memory-efficient few-step text-to-image diffusion models with metric-decoupled mixed precision quantization. In *ECCV*, 2024. [3](#)

Zheng, X., Liu, X., Bian, Y., Ma, X., Zhang, Y., Wang, J., Guo, J., and Qin, H. Bidm: Pushing the limit of quantization for diffusion models. In *NeurIPS*, 2024. [2](#)

Zheng, X., Liu, X., Qin, H., Ma, X., Zhang, M., Hao, H., Wang, J., Zhao, Z., Guo, J., and Magno, M. Binarydm: Accurate weight binarization for efficient diffusion models. In *ICLR*, 2025. [2](#)

Zhou, S., Wu, Y., Ni, Z., Zhou, X., Wen, H., and Zou, Y. Dorefa-net: Training low bitwidth convolutional neural networks with low bitwidth gradients. *arXiv preprint arXiv:1606.06160*, 2016. [2](#)

Zhu, L., Li, J., Qin, H., Li, W., Zhang, Y., Guo, Y., and Yang, X. Passionsr: Post-training quantization with adaptive scale in one-step diffusion based image super-resolution. In *CVPR*, 2025. [2](#), [7](#)